

STRUCTURE OF INORGANIC COMPOUNDS

Microstructure of the Al–La–Ni–Fe System

A. L. Vasil'ev^{a, b}, A. G. Ivanova^b, N. D. Bakhteeva^c, N. N. Kolobylna^a, A. S. Orekhov^b,
M. Yu. Presnyakov^a, and E. V. Todorova^c

^a National Research Centre “Kurchatov Institute”, pl. Akademika Kurchatova 1, Moscow, 123182 Russia

^b Shubnikov Institute of Crystallography, Russian Academy of Sciences,

Leninskii pr. 59, Moscow, 119333 Russia

e-mail: a.vasiliev56@gmail.com

^c Baikov Institute of Metallurgy and Materials Science, Russian Academy of Sciences,

Leninskii pr. 49, Moscow, 119991 Russia

Received February 14, 2014

Abstract—The microstructure of alloys based on the Al–La–Ni–Fe system, which are characterized by a unique ability to form metal glasses and nanoscale composites in a wide range of compositions, has been investigated. Al₈₅Ni₇Fe₄La₄ and Al₈₅Ni₉Fe₂La₄ alloys have been analyzed by electron microscopy (including high-resolution scanning transmission electron microscopy), energy-dispersive X-ray microanalysis, electron diffraction (ED), and X-ray diffraction (XRD). It is found that, along with fcc Al and Al₄La (Al₁₁La₃) particles, these alloys contain a ternary phase Al₃Ni_{1-x}Fe_x (sp. gr. *Pnma*) isostructural to the Al₃Ni phase and a quaternary phase Al₈Fe_{2-x}Ni_xLa isostructural to the Al₈Fe₂Eu phase (sp. gr. *Pbam*). The unit-cell parameters of the Al₃Ni_{1-x}Fe_x and Al₈Fe_{2-x}Ni_xLa compounds, determined by ED and refined by XRD, are $a = 0.664(1)$ nm, $b = 0.734(1)$ nm, and $c = 0.490(1)$ nm for Al₃Ni_{1-x}Fe_x and $a = 1.258(3)$ nm, $b = 1.448(3)$ nm, and $c = 0.405(8)$ nm for Al₈Fe_{2-x}Ni_xLa. In both cases Ni and Fe atoms are statistically arranged, and no ordering is found. Al₈Fe_{2-x}Ni_xLa particles contain inclusions in the form of Al₃Fe δ layers.

DOI: 10.1134/S1063774514060297

INTRODUCTION

A new class of Al–REM–TM aluminum alloys (REM indicates rare earth metal and TM is transition metal) was revealed in 1988 [1–4]. These alloys differ from conventional ones by their extraordinary ability to form metal glasses and nanoscale composites in a wide range of compositions. Having low density, these alloys possess unique mechanical characteristics and corrosion resistance (a property typical of aluminum alloys). Nanocomposites or amorphous alloys can be formed using different technologies; one of them, strong plastic deformation (SPD), was described in detail in [5]. The first attempts to fabricate nanocomposites from a polycrystalline Al–Ni–Fe–La alloy by this method were reported in [6]. The choice of alloying components (Ni, Fe, and La) is based on the fact that specifically Al–Ni–La alloys are characterized by a uniquely wide range of glass formation among many Al–REM–TM alloys [7]; note that the Fe additive not only widens this range, but also improves the mechanical characteristics of the alloys [8]. The microstructure of the final nanocomposite depends on the SPD conditions, the microstructure and phase composition of the initial material, and (especially) on the presence of intermetallic compounds (inclusions with high hardness and peculiar morphology, which may facilitate formation of a reinforcing mesh) [9]. However, the microstructure and phase composition of Al–Ni–

Fe–La alloys have been investigated poorly. Even the ternary phase diagrams of the Al–Fe–La, Al–Ni–La, and Al–Ni–Fe systems reported in [10–12] and some studies devoted to ternary compounds (specifically, Al₁₀Fe₂La [13]) do not yield a complete representation of possible crystalline phases existing in the Al–Ni–Fe–La system (in the Al-enriched region). All the cited studies contain no data on isostructural Al–Fe–La and Al–Ni–La alloys with identical or similar compositions in the Al-enriched regions of ternary diagrams, and the X-ray diffraction data on nanocrystalline Al–Ni–Fe–La alloys in the Al-enriched region [8, 14, 15] are contradictory. Phase analysis by electron microscopy (EM) and electron diffraction (ED) has not been performed either. Using optical microscopy, scanning EM (SEM), transmission EM (TEM), energy-dispersive X-ray microanalysis (EDXMA), and X-ray diffraction (XRD), it was shown in [6] that Al₈₅Ni_{11-x}Fe_xLa₄ alloys ($x = 2$ or 4 at %) contain four phases: (1) fcc Al, (2, 3) orthorhombic compounds Al₃Ni (with Ni atoms partially replaced by Fe atoms, i.e., Al₃Ni_{1-x}Fe_x) and Al₄La (Al₁₁La₃), and (4) a Fe-containing phase. However, the structure and composition of the latter were not identified, the character of substitution of Fe atoms for Ni in the Al₃Ni_{1-x}Fe_x phase was not established and no quantitative data were obtained, the unit-cell parameters were not refined, and the relative phase content in the alloys

was not found. At the same time, it is these phases that may control the mechanical properties of nanocomposites in the Al–Ni–Fe–La systems.

In this paper we report the results of studying the microstructure of three- and four-component phases in $\text{Al}_{85}\text{Ni}_{11-x}\text{Fe}_x\text{La}_4$ alloys ($x = 2$ or 4 at %) by SEM, transmission ED (TED), high-resolution TEM, scanning transmission EM (STEM), EDXMA, and XRD. The volume composition of phases in these alloys is estimated.

EXPERIMENTAL

Polycrystalline $\text{Al}_{85}\text{Ni}_7\text{Fe}_4\text{La}_4$ and $\text{Al}_{85}\text{Ni}_9\text{Fe}_2\text{La}_4$ alloys were obtained in the form of ingots from melts of corresponding compositions upon cooling in air. The surface of the samples was mechanically ground and investigated in a scanning electron–ion microscope (SEIM) Helios (FEI, United States) at an accelerating voltage of 2 kV. EDXMA was performed in the same instrument using a corresponding attachment (EDAX, United States) at an accelerating voltage of 15 kV. Samples for EM and ED were prepared by two methods: using (i) standard electropolishing in a Tenupol 5 system (Struers, United States) with subsequent etching by low-energy Ar^+ ions in a PIPS system (Gatan, United States) and (ii) a focused ion beam (FIB) in Helios SEIM. EM studies were performed in a transmission/scanning transmission electron microscope Titan 80–300 TEM/STEM (FEI, United States), equipped with a spherical aberration corrector (probe corrector), at an accelerating voltage of 300 kV. This configuration makes it possible to obtain STEM images with a resolution of 0.08 nm. The instrument is equipped with an EDXMA (EDAX, United States), a dark-field ring detector of electrons scattered by large angles (Fischione, United States), bright- and dark-field detectors for scanning microscopy, and electron energy-loss spectrometer (Gatan,

United States). Image processing was performed using the Digital Micrograph program (Gatan, United States). XRD studies were performed on plates about $4 \times 10 \text{ mm}^2$ in size grinded from one side.

XRD patterns of the samples were recorded on an XPertPro diffractometer (PANalytical) (CuK_α radiation, 40 kV, 35 mA, Ni filter) in the Bragg–Brentano (reflection) geometry using continuous triple scanning in the range of 2θ angles from 8° to 80° . The scan step and time were, respectively, 0.016 deg/s and 250 s. Phases were identified using the powder X-ray diffraction pattern database PDF-2. The phase composition was determined by full-profile least-squares refinement method using the PowderCell 2.4 program [16], with the simultaneous refinement of phase volume ratios, unit-cell parameters, scale factor, and components of diffraction-line broadening that are related to the size of coherent-scattering region.

OPTICAL MICROSCOPY, SEM, TEM, AND STEM DATA AND DISCUSSION

A typical optical-microscopy image of a surface lap of an $\text{Al}_{85}\text{Ni}_7\text{Fe}_4\text{La}_4$ sample is shown in Fig. 1. Different colors, contrasts, and morphological features of particles make it possible to distinguish four phases in the figure. Intermetallic compound particles reach several hundreds of micrometers in size and, judging from optical images, most of them are polycrystalline. As was shown in [6], the phase contents is the same in different samples, the difference is only in the sizes of intermetallic particles and their concentrations. An SEM image of the $\text{Al}_{85}\text{Ni}_7\text{Fe}_4\text{La}_4$ sample is shown in Fig. 2a and the EDXMA data on Al, Al–Ni–Fe, Al–La, and Al–Fe–Ni–La particles are listed in the table. EDXMA was carried out at a relatively high accelerating voltage (15 kV); therefore, one cannot exclude the influence of multiple scattering and formation of an additional signal from the Al matrix,

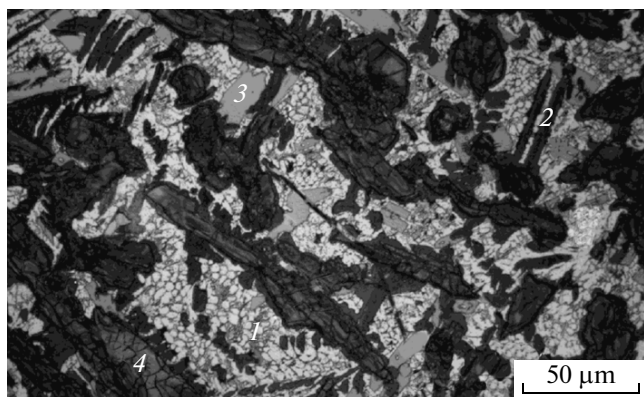


Fig. 1. Microstructure of the $\text{Al}_{85}\text{Ni}_7\text{Fe}_4\text{La}_4$ alloy (optical metallography data): (1) Al, (2) $\text{Al}_3\text{Ni}_{1-x}\text{Fe}_x$, (3) Al_4La ($\text{Al}_{11}\text{La}_3$), and (4) $\text{Al}_8\text{Fe}_{2-x}\text{Ni}_x\text{La}$.

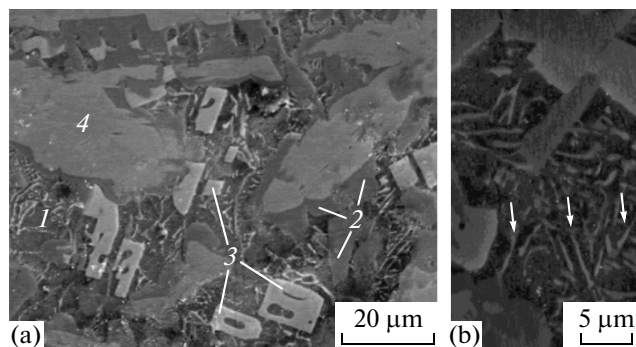


Fig. 2. (a) Secondary-electron SEM image of the $\text{Al}_{85}\text{Ni}_7\text{Fe}_4\text{La}_4$ alloy surface: (1) Al, (2) $\text{Al}_3\text{Ni}_{1-x}\text{Fe}_x$, (3) Al_4La ($\text{Al}_{11}\text{La}_3$), and (4) $\text{Al}_8\text{Fe}_{2-x}\text{Ni}_x\text{La}$; (b) an enlarged image, platelike Al_4La ($\text{Al}_{11}\text{La}_3$) particles are shown by arrows.

which shifts the ratio of the measured element content toward Al. The brightest contrast and faceting are observed for Al–La particles. The largest particles consist of a core, containing Al, La, Fe, and Ni (with a less bright contrast than Al–La), and a peripheral part, containing Al, Ni, and Fe and having an even darker contrast. An enlarged image of a sample region with Al- and La-containing particles which exhibit elongated platelike morphology is shown in Fig. 2b. It is possible that all La aluminide particles have a plate-like morphology, and different cross sections of these particles are observed in the cut.

A bright-field TEM image of a cut prepared using an FIB is shown in Fig. 3. A joint study using EDXMA and ED methods unambiguously indicated the presence of particles of four types: fcc Al; particles with a structure belonging to the orthorhombic system, Al_4La or $\text{Al}_{11}\text{La}_3$ [17, 18] (the unit-cell parameters and crystal structures of both compounds are similar and cannot be distinguished by ED); particles with a structure belonging to the orthorhombic $\text{Al}_3\text{Ni}_{1-x}\text{Fe}_x$ system, which is isostructural to Al_3Ni [19]; and particles with a composition close to $\text{Al}_8\text{Fe}_{2-x}\text{Ni}_x\text{La}$. $\text{Al}_3\text{Ni}_{1-x}\text{Fe}_x$ particles have another morphology: most often of line type, with an aspect ratio ranging from 2 : 1 to 10 : 1, and (more rarely) rounded up to 15 μm in size. According to the EDXMA data, the Al : Ni : Fe ratio is 78 : 17 : 6 (in at %). As was noted above, the excess of Al content above the stoichiometric composition Al : (Ni, Fe) = 3 : 1 may be related to signal reemission or superposition of the signal from $\text{Al}_3\text{Ni}_{1-x}\text{Fe}_x$ particles on the Al matrix signal. High-resolution ED and TEM studies of $\text{Al}_3\text{Ni}_{1-x}\text{Fe}_x$ particles did not reveal any traces of superstructure; i.e., the substitution of Fe atoms for Ni is statistical rather than ordered. The unit-cell parameters found by ED were close to those of Al_3Ni [19]. The statistical substitution of Fe and Co atoms for Ni was observed in Al–Y–(Gd)–Ni–Co–Fe alloys [20, 21].

A bright-field TEM image of a particle with a composition close to $\text{Al}_8\text{Fe}_{2-x}\text{Ni}_x\text{La}$ is shown in Fig. 4a. This and other images (for example, Fig. 3) demonstrate flat defects with a relatively high density; according to the image-based estimates, it amounts to $\sim 10^{14}\text{--}10^{15}\text{ cm}^{-3}$. An EDXMA study yielded the following ratios of element concentrations: Al : Fe : Ni : La = 7.2 : 1.0 : 0.9 : 1.0. Electron diffraction patterns from an isolated portion one of $\text{Al}_8\text{Fe}_{2-x}\text{Ni}_x\text{La}$ particles are shown in Figs. 4b–4d. Calculations of ED patterns showed that they coincide with a high accuracy with the electron diffraction patterns of the $\text{Al}_8\text{Fe}_2\text{Eu}$ compound [22] with [001], [101], and [102] zone axes. The structure of this compound belongs to the orthorhombic system with the sp. gr. *Pbam* and unit-cell parameters $a = 12.530(6)\text{ nm}$, $b = 14.503(4)\text{ nm}$, and $c = 4.036(1)\text{ nm}$ (Fig. 5). The ED pattern contains additional reflections in the $h00$ positions for $h = 2n + 1$ and $0l0$ positions for $l = 2n + 1$, which are for-

bidden for the sp. gr. *Pbam*. Eliminating dynamic effects by tilting the sample or using its thinned regions leads to the disappearance or significant attenuation of these reflections. Hence, these additional spots are due to double diffraction. Based on the ED data, one can conclude that the structure of the particles under study coincides with the structure of $\text{Al}_8\text{Fe}_2\text{Eu}$ intermetallic compound where Eu atoms are replaced with La atoms and Ni and Fe atoms are distributed statistically and occupy the 4g site. Thus, the particles studied can be described by the formula $\text{Al}_8\text{Fe}_{2-x}\text{Ni}_x\text{La}$, where, according to the EDXMA data, $x = 0.8\text{--}0.9$. ED patterns of Kessel type in a convergent beam, one of which is shown in Fig. 4e, and they also confirm that the compound under consideration can be described by the formula $\text{Al}_8\text{Fe}_{2-x}\text{Ni}_x\text{La}$ with unit-cell parameters close to those for $\text{Al}_8\text{Fe}_2\text{Eu}$. The ED patterns with a zone axis parallel to the $[h0l]^*$ directions

Particles	Al	Ni	Fe	La
Al	95 ± 2	1 ± 0.5	<1	5 ± 1
Al–Ni–Fe	78 ± 2	16 ± 2	6 ± 2	1 ± 0.5
Al–La	72 ± 2	3 ± 2	2 ± 2	22 ± 2
Al–Ni–Fe–La	72 ± 2	8 ± 1	10 ± 1	9 ± 1

The data are in at %.

bidden for the sp. gr. *Pbam*. Eliminating dynamic effects by tilting the sample or using its thinned regions leads to the disappearance or significant attenuation of these reflections. Hence, these additional spots are due to double diffraction. Based on the ED data, one can conclude that the structure of the particles under study coincides with the structure of $\text{Al}_8\text{Fe}_2\text{Eu}$ intermetallic compound where Eu atoms are replaced with La atoms and Ni and Fe atoms are distributed statistically and occupy the 4g site. Thus, the particles studied can be described by the formula $\text{Al}_8\text{Fe}_{2-x}\text{Ni}_x\text{La}$, where, according to the EDXMA data, $x = 0.8\text{--}0.9$. ED patterns of Kessel type in a convergent beam, one of which is shown in Fig. 4e, and they also confirm that the compound under consideration can be described by the formula $\text{Al}_8\text{Fe}_{2-x}\text{Ni}_x\text{La}$ with unit-cell parameters close to those for $\text{Al}_8\text{Fe}_2\text{Eu}$. The ED patterns with a zone axis parallel to the $[h0l]^*$ directions

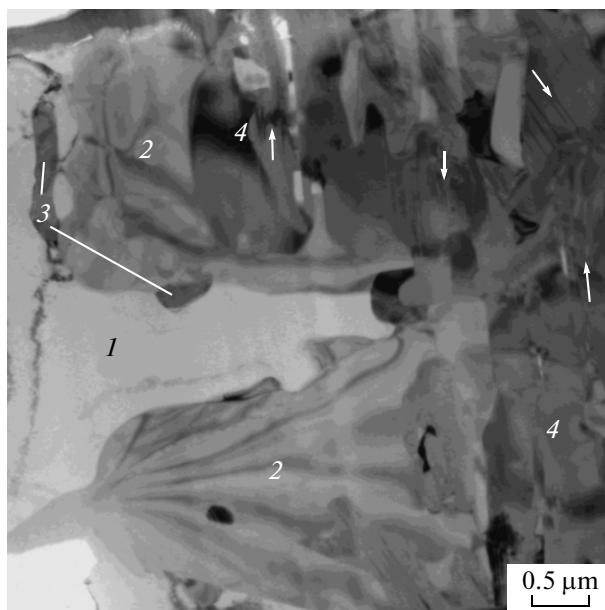


Fig. 3. Bright-field TEM image of the $\text{Al}_5\text{Ni}_7\text{Fe}_4\text{La}_4$ alloy microstructure: (1) Al, (2) $\text{Al}_3\text{Ni}_{1-x}\text{Fe}_x$, (3) Al_4La ($\text{Al}_{11}\text{La}_3$), and (4) $\text{Al}_8\text{Fe}_{2-x}\text{Ni}_x\text{La}$ (flat defects in particles are indicated by arrows).

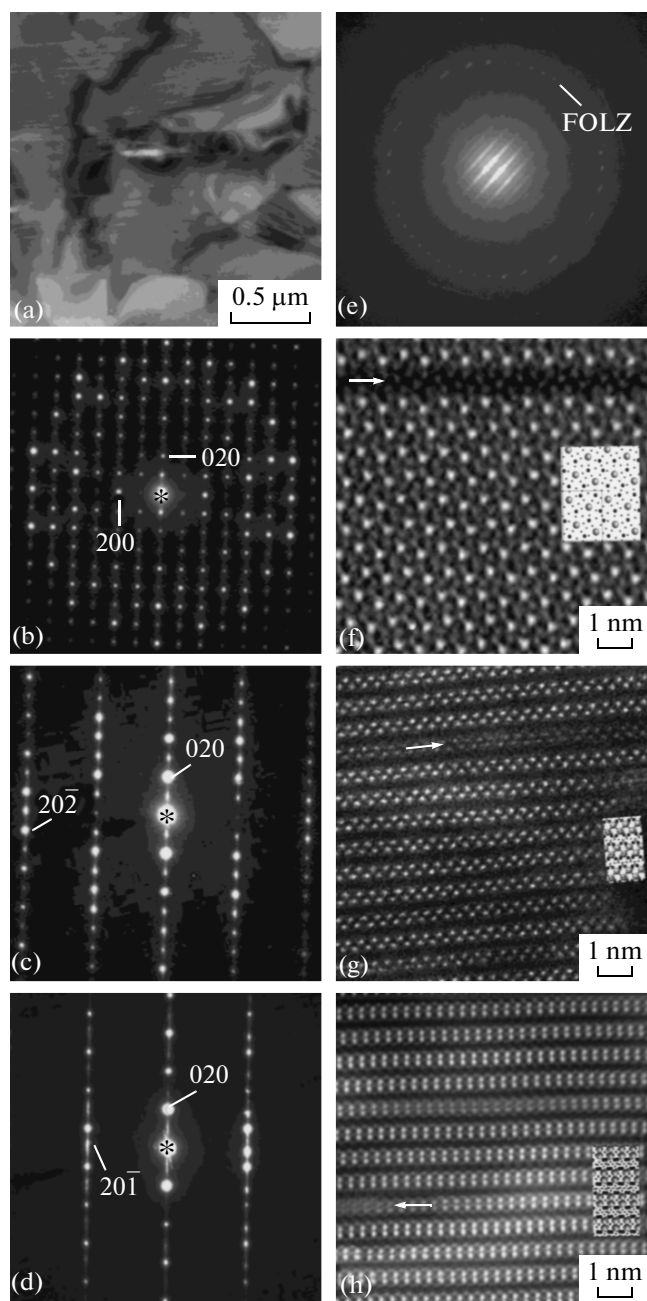


Fig. 4. TEM and ED data on $\text{Al}_8\text{Fe}_{2-x}\text{Ni}_x\text{La}$ particles. (a) Bright-field TEM image of a particle. (b–d) ED patterns from isolated regions of particles with (b) [001], (c) [101], and (d) [102] zone axes. (e) An electron diffraction pattern recorded in a convergent beam with the [102] zone axis. (f–h) Dark-field STEM images, obtained by recording electrons scattered at large angles, in the (f) (001), (g) (101), and (h) (102) projections.

exhibit rods along the reflections in the directions parallel to the b^* axis; these rods are formed from flat defects in the perpendicular direction. Specifically these defects manifest themselves as lines in bright-field TEM images; i.e., these are disk-shaped defects

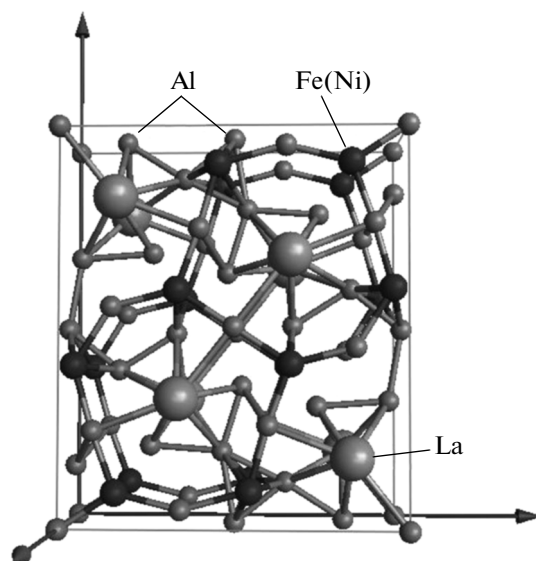


Fig. 5. Schematic diagram of the unit cell of $\text{Al}_8\text{Fe}_{2-x}\text{Ni}_x\text{La}$ crystal; Fe and Ni atoms are denoted similarly.

with a habit plane parallel to the (010) axis of the crystal structure. Bright-field TEM images and dark-field STEM images, recorded with a resolution at the lattice level (Figs. 4f–4h), indicate that the thickness of disk-shaped defects is close to the unit-cell parameter $b/2$ of the $\text{Al}_8\text{Fe}_{2-x}\text{Ni}_x\text{La}$ crystal. The structure of these defects was investigated by high-resolution STEM with the detection of electrons scattered by large angles. One of these images with a zone axis $B = [001]$ is shown in Fig. 6a, where the brightest spots correspond to columns of La atoms, because these atoms have the largest atomic number Z . The spots corresponding to Ni and Fe atoms are less bright. Superposing the $\text{Al}_8\text{Fe}_{2-x}\text{Ni}_x\text{La}$ structure on an image of a defect-free portion showed their complete correspondence. The interpretation of the $\text{Al}_8\text{Fe}_{2-x}\text{Ni}_x\text{La}$ structure (shown schematically in Fig. 6b) allowed us to make some suggestions about the structure of flat defects. The areas in the images that correspond to defects contain the brightest spots due to La atoms; therefore, one can suggest the presence of Al–Ni, Al–Fe, or Al–Ni–Fe intermetallic compounds near defects. The stoichiometric ratio in this intermetallic compound, Al : (Ni, Fe), is likely close to the ratio between Al and other atoms in the particles under study: 8 : 3. Note that the contrast in the high-resolution STEM images, obtained by recording electrons scattered by large angles, very closely reproduces the object crystal structure, and the atomically resolved images of defects can be directly compared with the structures of Al_3Ni [19], $\text{Al}_{5.4}\text{Fe}_2$ [23], $\text{Al}_{5.6}\text{Fe}_2$ [24], Al_3Fe [25], $\text{Al}_{13}\text{Fe}_4$ [26], $\text{Fe}_{4-x}\text{Ni}_x\text{Al}_{10}$, and $\text{Fe}_{2-x}\text{Ni}_x\text{Al}_9$ (τ_2) [12] intermetallic compounds in certain orientations. This comparison made it possible to determine

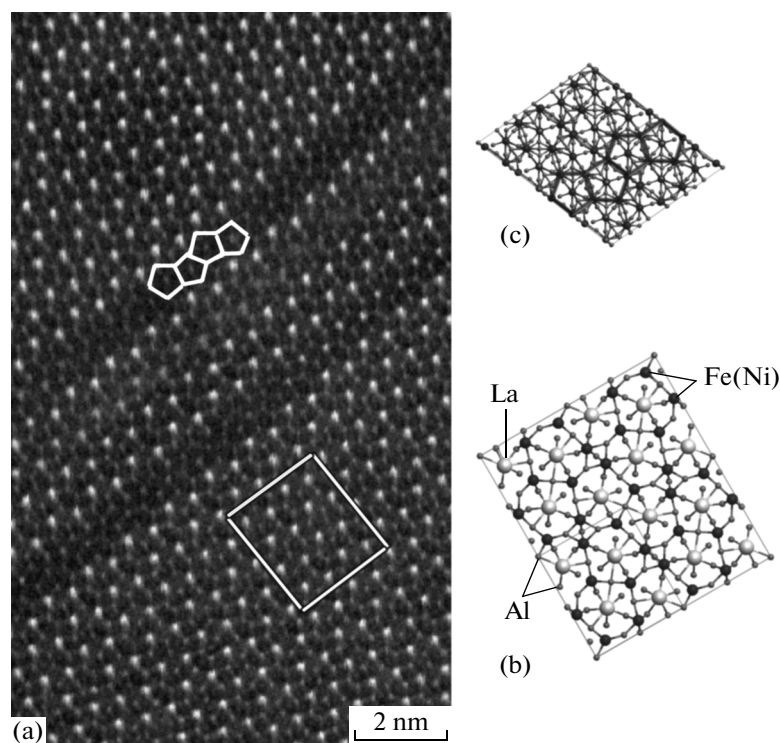


Fig. 6. (a) Dark-field STEM image (obtained by recording electrons scattered at large angles) of the $\text{Al}_8\text{Fe}_{2-x}\text{Ni}_x\text{La}$ lattice with the zone axis $B = [001]$; 2×2 unit cells are selected. Pentagons formed by Fe and Ni atoms in Al_3Fe inclusions are shown. (b) Schematic of the $\text{Al}_8\text{Fe}_{2-x}\text{Ni}_x\text{La}$ lattice in the (001) projection. (c) Schematic of the Al_3Fe_2 lattice in the (010) projection. Black lines indicate pentagons formed by Fe and Ni atoms; they correspond to the pentagons in the experimental image in panel a.

the intermetallic compound with the closest structure: Al_3Fe (monoclinic system, sp. gr. $C2/m$), which forms disk-shaped defects, incorporated into the $\text{Al}_8\text{Fe}_{2-x}\text{Ni}_x\text{La}$ intermetallic compound in the form of δ layers. The structural images of these inclusions reveal clear pentagons composed of either Fe or Ni atoms, with an atom of the same element in the center. These pentagons are selected in the STEM image in Fig. 6a. Because of the small atomic number Z_{Al} , the contrast from columns of Al atoms is very low and can barely be distinguished in these images. The transverse size of inclusions is smaller than the unit-cell parameter of Al_3Fe in the direction perpendicular to the (010) plane:

$$a \cos(\beta - 90^\circ) \approx 1.55 \text{ nm}, \quad \cos 27.7^\circ \approx 1.37 \text{ nm}$$

(a and β are the unit-cell parameters of Al_3Fe). However, when considering a reduced (or minimum) Al_3Fe cell ($a = 0.8078 \text{ nm}$, $b = 0.8735 \text{ nm}$, $c = 0.12471 \text{ nm}$, $\alpha = 105.630^\circ$, $\beta = 89.999^\circ$, and $\gamma = 117.538^\circ$), one reveals complete coincidence with the structure of an Al_3Fe monolayer (δ layer). Similar defects (monoclinic inclusions in $\text{Al}_{19}\text{Y}_3\text{Ni}_5$ intermetallic compounds with orthorhombic structure) were observed previously in [27]; however, the thickness of these inclusions was not limited to one unit-cell parameter.

STEM images made it possible to derive orientation relationships between the $\text{Al}_8\text{Fe}_{2-x}\text{Ni}_x\text{La}$ matrix and the Al_3Fe compound:

$$\begin{aligned} (001)_{\text{Al}_8\text{Fe}_{2-x}\text{Ni}_x\text{La}} \parallel (010)_{\text{Al}_3\text{Fe}}, \\ [100]_{\text{Al}_8\text{Fe}_{2-x}\text{Ni}_x\text{La}} \parallel [001]_{\text{Al}_3\text{Fe}}. \end{aligned}$$

The X-ray diffraction data on the samples of $\text{Al}_{85}\text{Ni}_7\text{Fe}_4\text{La}_4$ and $\text{Al}_{85}\text{Ni}_9\text{Fe}_2\text{La}_4$ alloys are presented in Figs. 7a and 7b, respectively. A full-profile analysis of the XRD patterns of both alloys revealed the presence of five phases in $\text{Al}_{85}\text{Ni}_7\text{Fe}_4\text{La}_4$ alloy: fcc Al; orthorhombic $\text{Al}_3\text{Ni}_{1-x}\text{Fe}_x$ and Al_4La (or $\text{Al}_{11}\text{La}_3$) phases; the monoclinic Al_3Fe phase; and the $\text{Al}_8\text{Fe}_{2-x}\text{Ni}_x\text{La}$ intermetallic phase, isostructural to the Al_8FeEu intermetallic compound. For the $\text{Al}_{85}\text{Ni}_7\text{Fe}_4\text{La}_4$ alloy, the best agreement between the experimental and theoretical XRD patterns (weighting profile refinement R factor $wR_p = 3.7\%$) was obtained for the following (in vol %) composition: Al(47%)– Al_3Ni (24%)– Al_4La (14%)– $\text{Al}_8\text{Fe}_2\text{La}$ (12%)– Al_3Fe (2.5%).

The XRD pattern of the $\text{Al}_{85}\text{Ni}_9\text{Fe}_2\text{La}_4$ alloy contains an anomalously strong (210) Al_3Ni reflection, which may be related to the preferred orientation of grains of one of the main phases in the Al(30%)– Al_3Ni (62%)– Al_4La (4%)– $\text{Al}_8\text{Fe}_2\text{La}$ (4%) composi-

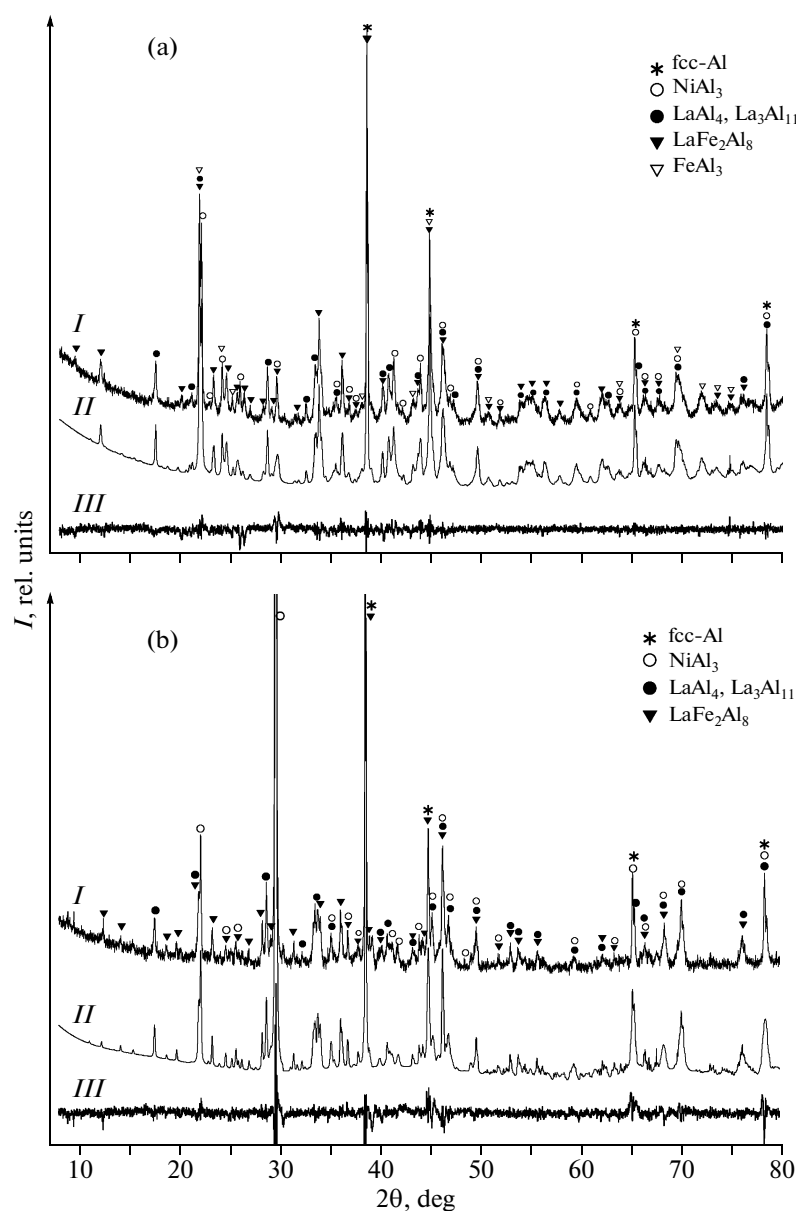


Fig. 7. XRD patterns of (a) $\text{Al}_{85}\text{Ni}_7\text{Fe}_4\text{La}_4$ and (b) $\text{Al}_{85}\text{Ni}_9\text{Fe}_2\text{La}_4$ (*I* alloys (*I*, *II*, and *III* are, respectively, an experimental diffraction pattern, a theoretical profile, and a difference profile).

tion ($R_{wp} = 6.04\%$). The Al_3Fe phase was not revealed in this sample, which is likely related to the lower density and smaller size of $\text{Al}_8\text{Fe}_{2-x}\text{Ni}_x\text{La}$ particles.

It was necessary to refine parameters for the following two phases in both alloys: the $\text{Al}_3\text{Ni}_{1-x}\text{Fe}_x$ phase, where about 25% Ni atoms are replaced with Fe atoms, and the $\text{Al}_8\text{Fe}_{2-x}\text{Ni}_x\text{La}$ phase. The refined parameters of $\text{Al}_3\text{Ni}_{1-x}\text{Fe}_x$ phase are as follows: $a = 0.664(1)$ nm, $b = 0.734(1)$ nm, and $c = 0.490(1)$ nm; for the $\text{Al}_8\text{Fe}_{2-x}\text{Ni}_x\text{La}$ phase, we obtained $a = 1.258(3)$ nm, $b = 1.448(3)$ nm, and $c = 0.405(8)$ nm. Comparing the XRD and EM data, we can suggest

that the Al_3Fe phase exists in the form of inclusions in $\text{Al}_8\text{Fe}_{2-x}\text{Ni}_x\text{La}$ particles.

CONCLUSIONS

The study of two polycrystalline $\text{Al}_{85}\text{Ni}_7\text{Fe}_4\text{La}_4$ and $\text{Al}_{85}\text{Ni}_9\text{Fe}_2\text{La}_4$ alloys by EM, ED, XRD, and EDXMA revealed that, along with fcc Al and Al_4La ($\text{Al}_{11}\text{La}_3$) particles, these alloys contain a ternary phase $\text{Al}_3\text{Ni}_{1-x}\text{Fe}_x$ isostructural to the Al_3Ni phase and a quaternary phase $\text{Al}_8\text{Fe}_{2-x}\text{Ni}_x\text{La}$ isostructural to the $\text{Al}_8\text{Fe}_2\text{Eu}$ phase. The space groups of these phases are $Pnma$ and $Pbam$, respectively. The unit-cell param-

ters are $a = 0.664(1)$ nm, $b = 0.734(1)$ nm, and $c = 0.490(1)$ nm for the $\text{Al}_3\text{Ni}_{1-x}\text{Fe}_x$ compound and $a = 1.258(3)$ nm, $b = 1.448(3)$ nm, and $c = 0.405(8)$ nm for the Al_8FeNiLa compound. In both cases the arrangement of Ni and Fe atoms is statistical; no ordering was found. The $\text{Al}_8\text{Fe}_{2-x}\text{Ni}_x\text{La}$ particles contain inclusions in the form of Al_3Fe δ layers.

ACKNOWLEDGMENTS

This study was supported by the Russian Foundation for Basic Research, project no. 13-02-12190 ofi-m.

REFERENCES

1. A. Inoue, K. Ohtera, A. P. Tsai, and T. Masumoto, *Jpn J. Appl. Phys.* **27**, 280 (1988).
2. A. Inoue, K. Ohtera, A. P. Tsai, and T. Masumoto, *Jpn J. Appl. Phys.* **27**, 479 (1988).
3. A. Inoue, K. Ohtera, A. P. Tsai, and T. Masumoto, *Jpn J. Appl. Phys.* **27**, 736 (1988).
4. Y. He, J. Poons, and G. J. Shiflet, *Science* **241**, 1640 (1988).
5. A. P. Zhilyaev and T. G. Langdon, *Prog. Mater. Sci.* **53**, 893 (2008).
6. N. D. Bakhteeva, E. V. Todorova, N. N. Kolobylyna, et al., *Metally*, No. 2, 55 (2013).
7. A. Inoue and A. Takeuchi, *Mater. Sci. Eng. A* **375–377**, 16 (2004).
8. R. Li, W.-M. Wang, H.-J. Ma, et al., *Nonferrous Met. Soc. China* **21**, 80 (2011).
9. A. L. Vasiliev, M. Aindow, M. J. Blackburn, and T. J. Watson, *Intermetallics* **12** (4), 349 (2004).
10. V. Raghavan and J. Phase, *Equilibria* **22**, 566 (2001).
11. V. Raghavan and J. Phase, *Equilibria* **27**, 392 (2006).
12. I. Chumak, K. W. Richter, and H. Ipser, *Intermetallics* **15**, 1416 (2007).
13. V. M. T. Thiede, T. Ebel, and W. Jeitschko, *J. Mater. Chem.* **8** (1), 125 (1998).
14. J. S. Kim, O. T. H. Nguyen, P. P. Choi, et al., *Chem. Sustainable Dev.* **15**, 175 (2007).
15. P. P. Choi, J. S. Kim, O. T. H. Nguyen, et al., *Mater. Sci. Eng.* **449**, 1119 (2007).
16. W. Kraus and G. Nolzeb, *J. Appl. Crystallogr.* **29** (3), 301 (1996).
17. I. I. Zalutskii and P. I. Kripyakevich, *Dopovidi Akad. Nauk Ukrain's'koi RSR, A: Fiz.-Tekh. Mat. Nauki* 362 (1967).
18. A. H. Gomes de Mesquita and K. H. J. Buschow, *Acta Crystallogr.* **22**, 497 (1967).
19. A. J. Bradley and A. Taylor, *Philos. Mag.* **23**, 1049 (1937).
20. A. L. Vasiliev, M. Aindow, M. J. Blackburn, and T. J. Watson, *Scr. Mater.* **52**, 699 (2005).
21. N. J. Magdefrau, A. L. Vasiliev, M. Aindow, et al., *Scr. Mater.* **51**, 485 (2004).
22. M. B. Manyako, I. N. Stets, I. V. Kivach, et al., *Dopovidi Akad. Nauk Ukrain's'koi RSR, B: Geol. Khim. Biol. Nauki* 39 (1983).
23. K. Schubert, U. Roesler, M. Kluge, et al., *Naturwissenschaften* **40** (16), 437 (1953).
24. U. Burkhardt, Yu. Grin, N. M. Ellner, and K. Peters, *Acta Crystallogr. B* **50**, 313 (1994).
25. P. J. Black, *Acta Crystallogr.* **8**, 43 (1955).
26. J. Grin, U. Burkhardt, M. Ellner, and K. Peters, *Z. Kristallogr.* **209**, 479 (1994).
27. A. Vasiliev, M. Aindow, M. J. Blackburn, and T. J. Watson, *Intermetallics* **12** (4), 349 (2004).

Translated by Yu. Sin'kov